Vol.48 No.1　2024

Journal

JOURNAL OF THE MAGNETICS SOCIETY OF JAPAN

TOEI

世界初！
高温超電導型VSM

新製品

世界初*、高温超電導マグネットをVSMに採用することで
測定速度 当社従来機1/20を実現。
0.5mm cube磁石のBr, HcJ高精度測定が可能と
なりました。

*2014年7月 東英工業調べ

測定結果例

高温超電導VSMによるNdFeB（sint.）0.5mm cube BHカーブ

磁化測定レンジ：0.2emu
Br = 13.2kG　　　　HcJ = 17.2kOe

高温超電導VSMによるNdFeB（sint.）1mm cube BHカーブ
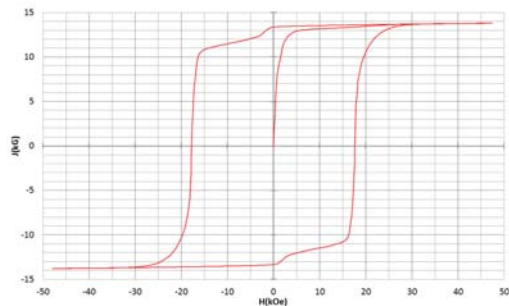
磁化測定レンジ：2emu
Br = 13.3kG　　　　HcJ = 17.7kOe

高温超電導VSMによるNdFeB（sint.）4mm cube BHカーブ
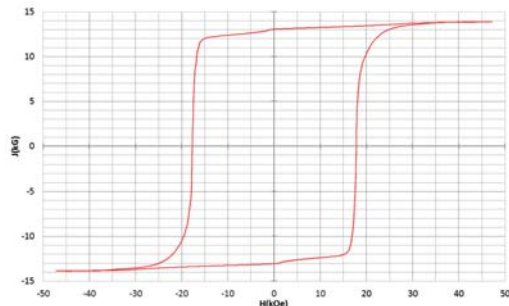
磁化測定レンジ：100emu
Br = 13.1kG　　　　HcJ = 17.8kOe

高速測定を実現

高温超電導マグネット採用により、高速測定を
実現しました。Hmax＝5Tesla, Full Loop測定が
2分で可能です。
（当社従来機：Full Loop測定 40分）

小試料のBr,HcJ高精度測定

0.5mm cube磁石のBr,HcJ高精度測定ができ、
表面改質領域を切り出しBr,HcJの強度分布等、
微小変化量の比較測定が可能です。
また、試料の加工劣化の比較測定が可能です。

試料温度可変測定

－50℃～＋200℃温度可変UNIT（オプション）

磁界発生部の小型化

マグネットシステム部寸法：0.8m×0.3m×0.3m

TOEI 東英工業株式会社

http://www.toeikogyo.co.jp

〒194-0035 東京都町田市忠生1-8-13
TEL：042-791-1211 FAX：042-792-0490
E-mail：sales@toeikogyo.co.jp

Journal of the Magnetics Society of Japan
Vol. 48, No. 1

CONTENTS

<Paper>

Induced pulse voltage and hysteresis loss during magnetization reversal of Wiegand wire

Fei Xue, Chao Yang*, Zenglu Song*, and Yasushi Takemura

Division of Electrical and Computer Engineering, Yokohama National University, *Yokohama 240-8501, Japan*
*School of Electrical Engineering, Nanjing Vocational University of Industry Technology, *Nanjing 210023, China*

When an alternating magnetic field is applied to a Wiegand wire, a series of pulse voltages are induced in a pickup coil due to fast magnetization reversal known as the large Barkhausen jump. This study aims to analyze the characteristics of the pulse voltage, including its height and area, which are determined from the intensity and frequency of the applied alternating magnetic field. We quantified the energy generated by magnetization reversal in a Wiegand wire. To achieve this, it was necessary to measure the energy consumed by a load resistor connected to the pickup coil. Additionally, we clarified the energy loss in the Wiegand wire.

Key words: Wiegand wire, Wiegand effect, large Barkhausen jump, magnetization reversal, electricity generator.

1. Introduction

Recent innovations in electronics have enabled the development of low-energy-consuming and battery-less devices. Wiegand sensors[1-2], which generate a pulse voltage during magnetization reversal of the magnetic wire installed in the sensors, are expected to find application in various self-powered modules[3]. These sensors are commercially available and have recently been used as a power source in battery-free rotary encoders[4]. This in turn has necessitated the evaluation of Wiegand sensors, particularly in terms of circuit applications and energy losses in the circuit.

The fast magnetization reversal in a Wiegand wire induces a pulse voltage in the pickup coil wound around the wire[5-6]. This reversal is accompanied by a large Barkhausen jump[7-9]. The amplitude and width of the induced pulse voltage, known as the Wiegand pulse, are independent of the frequency of the applied magnetic field[10]. The energy associated with the output pulse voltage generated by the Wiegand sensor can be used as a power supply for equipment without batteries[11-14]. The application of Wiegand sensors as receiving coils in wireless power transfer has also been reported[15].

Previous research has investigated the energy produced by the Wiegand sensor as an electricity generator and the power transferred to the Wiegand sensor when it is used as a receiver coil in wireless power transfer[10,15]. However, the relationship between the energy consumption and energy loss remains unclear. This study seeks to evaluate the energies of the induced pulse voltage, the loss in the Wiegand sensor, and the power consumption of the load resistance. We quantified the energy and loss, as well as the efficiency of the energy consumed in the load resistance.

2. Methods and Materials

The Wiegand sensor used in this study comprised a Wiegand wire (11 mm long and 0.25 mm in diameter) and a pickup coil of 3000 turns wound around the wire. Two ferrite beads (3 mm long, 1.3 mm in inner diameter, and 3.5 mm in outer diameter) were attached at both ends of the wire to concentrate the applied magnetic field to the wire (Fig. 1). The atomic composition of the Wiegand wire was $Fe_{0.4}Co_{0.5}V_{0.1}$. Other specifications and characterizations of the Wiegand sensor have been documented in prior research[16]. As shown in Fig. 1, a magnetic field generated by an excitation coil was externally applied to the sensors. An alternating current (AC) magnetic field of $\mu_0 H = 3–13$ mT at 10–1000 Hz was applied in this experiment.

A series of pulses of alternating positive and negative voltages were induced in the pickup coil when an AC magnetic field was applied to the Wiegand sensor. Figure 2 shows a typical waveform of a positive pulse voltage. An AC magnetic field of $\mu_0 H = 5$ mT was applied at 1 kHz. The output voltage V_{output} comprised two components, $V_{Wiegand}$ and $V_{induced}$, as shown in the figure. $V_{Wiegand}$ is the
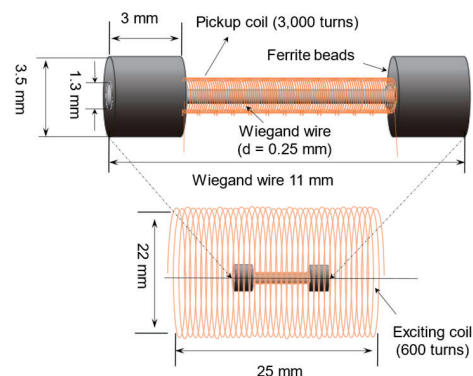
Fig. 1 Structure of Wiegand sensor. AC magnetic field generated by exciting coil is applied to Wiegand sensor.

Corresponding author: Yasushi Takemura
(e-mail: takemura-yasushi-nx@ynu.ac.jp).
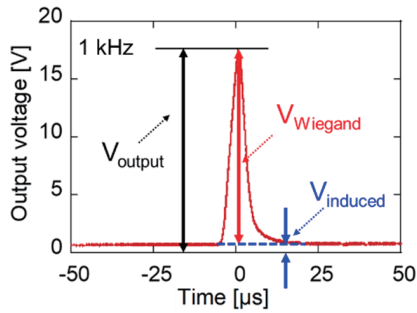
Fig. 2 Typically measured output voltage (black, V_{output}) induced in pickup coil. AC magnetic field of $\mu_0 H$ = 5 mT at 1 kHz was applied. Output voltage consists of 2 components: Wiegand pulse voltage (red, $V_{Wiegand}$) and induced voltage from applied AC magnetic field (blue, $V_{induced}$).

Fig. 4 Applied field frequency dependence of Wiegand pulse area. AC magnetic field of $\mu_0 H$ = 3–13 mT at 10–1000 Hz was applied. Amplitudes of positive and negative output voltages induced in Wiegand sensor. AC magnetic field of $\mu_0 H$ = 3–13 mT at 10–1000 Hz was applied.

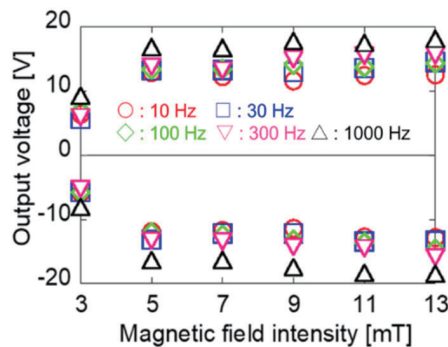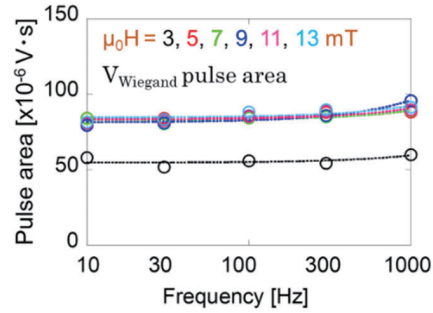Wiegand pulse voltage, while $V_{induced}$ is the voltage induced by the applied magnetic field. The pulse width was approximately 10 µs and independent of the frequency of the applied magnetic field, which was a unique feature in the magnetization reversal of the Wiegand wire.

Figure 3 shows the amplitude of the output voltage V_{output}. An AC magnetic field of $\mu_0 H$ = 3–13 mT was applied at 10–1000 Hz. The amplitudes of the positive and negative pulses are asymmetrical. There remains a region of a higher coercive force in the wire, which does not contribute to the large Barkhausen jump. The magnetization of this region is not reversed. The magnetization of the region exhibiting a large Barkhausen jump is alternately reversed. The magnetizations of these two regions can be either parallel or antiparallel[5], and the magnetostatic coupling between the regions is asymmetric, resulting in asymmetric positive and negative voltages. The output voltage increases with the intensity of the applied AC magnetic field. This dependence is due to an increase in the volume of magnetization reversal in the Wiegand wire. The amplitude of the pulse voltage increases slightly with the

applied field frequency, which is attributed to the voltage induced by the applied AC field, $V_{induced}$. The amplitude of the Wiegand pulse voltage, $V_{Wiegand}$, is independent of the frequency.

The area of the voltage pulse waveform in units of [V·s] corresponds to the energy. Figure 4 shows the area of the Wiegand pulse voltage, $V_{Wiegand}$. The induced voltage $V_{induced}$ was not included in the calculation of the pulse area. The area of the Wiegand pulse was not dependent on the applied field frequency. The area was almost constant for an applied field intensity above $\mu_0 H$ ≥ 5 mT, which agrees with the result shown in Fig. 3.

3. Experimental results and discussion

3.1 Energy consumption by load resistance

This section discusses the energy consumed by the load resistance connected to the Wiegand sensor. We prepared a circuit comprising a series connection of the pickup coil of the Wiegand sensor and the load resistance R (Fig. 5). The output voltage across the load resistance was measured, and the energy consumption was calculated as described later. The DC resistance of the Wiegand sensor

Fig. 3 Amplitudes of positive and negative output voltages induced in Wiegand sensor. AC magnetic field of $\mu_0 H$ = 3–13 mT at 10–1000 Hz was applied.

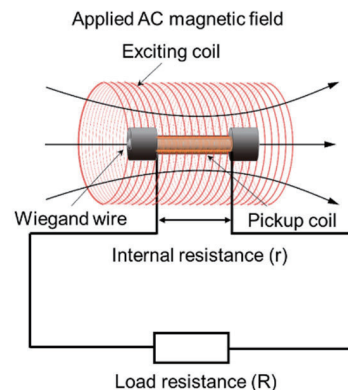**Fig. 5** Experimental circuit to study energy consumption at load resistance connected to Wiegand sensor.

(dominated by the pickup coil resistance) was $r = 273\ \Omega$. This is the internal resistance of the Wiegand sensor used as a power source. The load resistance was varied in the range of $R = 30$–$1000\ \Omega$.

The electric energy consumption by the load resistance $R = 100\ \Omega$ during one cycle of the applied AC magnetic field, E_{output}, was calculated using Eq. (1).

$$E_{\text{output}} = \int_0^T \frac{(V_{\text{output}}(t))^2}{R}\, dt \qquad (1)$$

The output voltage V_{output} in Fig. 2 is equivalent to the voltage across the load resistance. T is the period of the applied AC magnetic field. Two positive and negative pulses were generated during this period. Figure 6(a) shows the energy consumption by the load resistance E_{output} depending on the applied field frequency. It increases with increasing the applied field frequency, and is of the order of 0.1 µJ at 10 Hz and 1 µJ at 1 kHz. E_{output} is equivalent to the summation of the generated energy associated with the Wiegand pulse E_{Wiegand} and the induced voltage E_{induced}. E_{Wiegand} was calculated using Eq.

(2).

$$E_{\text{Wiegand}} = \int_0^T \frac{(V_{\text{output}}(t) - V_{\text{induced}}(t))^2}{R}\, dt \qquad (2)$$

As shown in Fig. 6(b), E_{Wiegand} is essentially independent of the applied field frequency, which is a specific feature of the large Barkhausen jump. However, the reason for the slight increase in E_{Wiegand} at 1 kHz is not clear. It was also confirmed that E_{induced} was proportional to the frequency, based on Faraday's law of induction (Fig. 6(c)).

3.2 Relationship of energy consumption with resistances and hysteresis loss

Figure 7 shows the minor hysteresis loop of the Wiegand wire derived from the output voltage induced in the pickup coil. An AC magnetic field of $\mu_0 H = 7$ mT in amplitude at 1 kHz was applied. A Barkhausen jump was observed at an applied field intensity of $\mu_0 H = \pm 2$–3 mT.

The closed area of the hysteresis loop corresponding to the hysteresis loss was calculated. Figure 8 shows the energy associated with the hysteresis loss during one cycle of the applied alternating magnetic field at 1 kHz. The skin depth at 1 kHz was calculated as 4.9 mm, which was larger than the radius of the Wiegand wire (0.125 mm). Therefore, the eddy current loss in the wire was negligible. The hysteresis loss increased with the intensity of the applied AC magnetic field in the range of $\mu_0 H = 0$–13 mT.

(a) E_{output}

(b) E_{Wiegand}

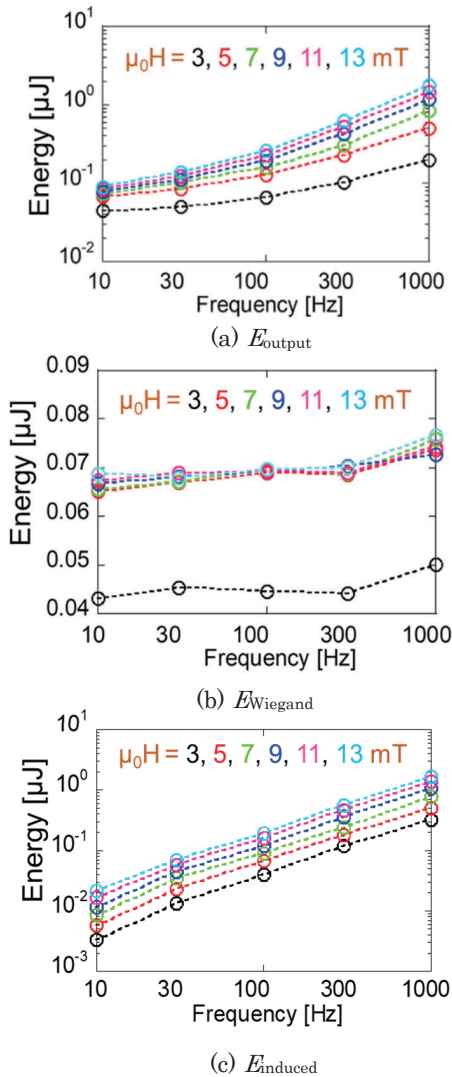(c) E_{induced}

Fig. 6 Electric energy consumption: (a) E_{output}, (b) E_{Wiegand}, and (c) E_{induced}.
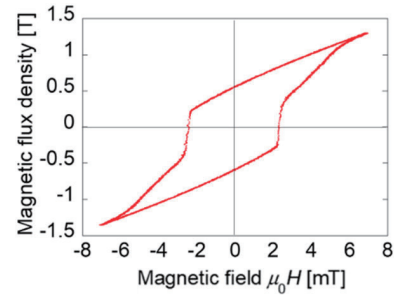

Fig. 7 Hysteresis loop of Wiegand wire derived from induced output voltage in pickup coil.
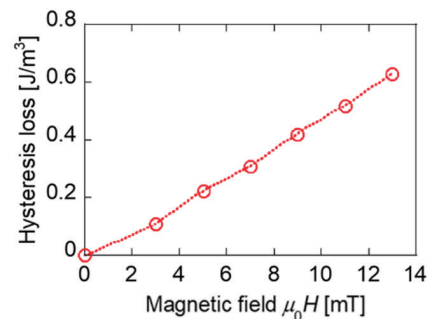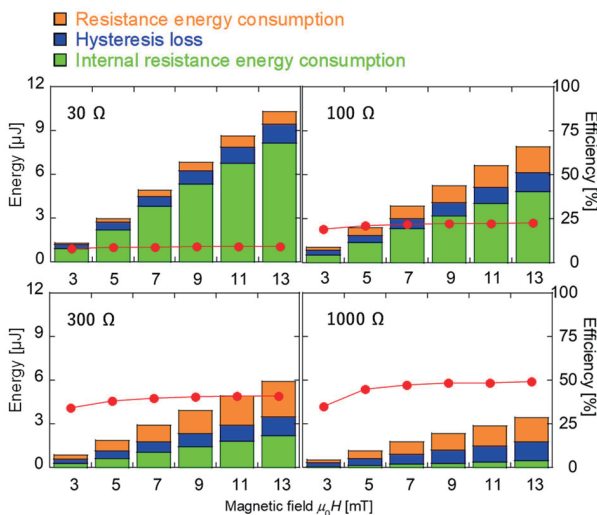

Fig. 8 Energy associated with hysteresis loss in Wiegand wire during one cycle of applied alternating magnetic field depending on field intensity.

Finally, we analyzed the energy consumption of the entire circuit shown in Fig. 5. Figure 9 shows the energy consumption by the load resistance E_{load} and internal resistance $E_{internal}$ during one cycle of the applied AC magnetic field of $\mu_0 H = 3–13$ mT at 1 kHz. The connected load resistances were $R = 30, 100, 300,$ and 1000 Ω. Because the load and internal resistances were series-connected, the ratio $E_{load}/E_{internal}$ equaled that of these resistances. The hysteresis loss, $E_{hysteresis}$, is also shown in Fig. 9. It was calculated from the area of a minor hysteresis loop (shown in Fig. 7), which was derived from the open circuit voltage induced in the pickup coil. In the experimental setup shown in Fig. 5, the energy supplied from the excitation coil to the circuit including the pickup coil and Wiegand wire is not considered as the input energy. As the intrinsic value of the hysteresis loss should not depend on the load resistance, $E_{hysteresis}$ increases monotonically with increasing the applied field intensity.

As shown in Fig. 9, the E_{load} for $R = 300$ Ω is larger than those for the other resistances. This is due to the impedance matching between the load resistance and the internal resistance of 273 Ω. E_{load}, $E_{hysteresis}$, and $E_{internal}$ increase with the applied field intensity. The energy efficiency of the load resistance against the total energy consumption is a significant parameter for practical applications. Figure 9 also shows the energy efficiency calculated using $E_{load} / (E_{load} + E_{hysteresis} + E_{internal})$. The efficiencies are approximately 8, 24, 40, and 47% for $R = 30, 100, 300,$ and 1000 Ω, respectively. They remain almost constant regardless of the applied field intensity for $\mu_0 H \geq 5$ mT. They increase with increasing R, which is due to less energy consumption at the internal resistance with less current through the circuit.

4. Conclusion

We measured the output voltage induced in a pickup coil during fast magnetization reversal in a Wiegand wire and analyzed its energy, which was available in a load resistance connected to the pickup coil. The output voltage, V_{output}, was composed of the voltage originated from the Wiegand pulse, $V_{Wiegand}$, and the voltage induced by the applied alternating magnetic field, $V_{induced}$. $V_{Wiegand}$ and its pulse area were independent of the frequency of the applied field, whereas $V_{induced}$ was proportional to the frequency. We determined the energy consumption in the load resistance, E_{load} to be approximately 0.07 µJ. We also quantified the energy losses in the internal resistance of the Wiegand sensor and energy consumed as the magnetization hysteresis loss of the Wiegand wire. The energy efficiency calculated by the ratio of the energy consumed by the load resistance and energy generated in the Wiegand sensor was also determined to be approximately 8–47% depending on the load resistance.

References

1) J. R. Wiegand and M. Velinsky: U.S. Patent #3,820,090, (1974).
2) P.E. Wiegand: *Electronics*, **48**, 100 (1975).
3) C.-C. Lin, Y.-C. Tseng, and T.S. Chin: *Magnetochem.*, **8**, 128 (2022).
4) Products, Wiegand sensor, POSITAL: https://www.posital.com/en/products/wiegand-sensors/wiegand-sensors.php.
5) S. Abe and A. Matsushita: *IEEE Trans. Magn.*, **31**, 3152 (1995).
6) F. Iob, S. Saggini, M. Ursino, and Y. Takemura: *IEEE Trans. Emerg. Sel. Topics Power Electron.*, **11**, 372 (2023).
7) N. Yano, S. Furukawa, K. Oka, I. Ogasawara, J. Yamasaki, and F.B. Humphrey: *IEEE Trans. Magn.*, **32**, 4532 (1996).
8) R. Malmhall, K. Mohri, F.B. Humphrey, T. Manabe, H. Kawamura, J. Yamasaki, and I. Ogasawara: *IEEE Trans. Magn.*, **23**, 3242 (1987).
9) M. Vázquez, C. Gómez-Polo, D.-X. Chen, and A. Hernando: *IEEE Trans. Magn.*, **30**, 907 (1994).
10) Y. Takemura, N. Fujinaga, A. Takebuchi, and T. Yamada: *IEEE Trans. Magn.*, **53**, 4002706 (2017).
11) H.-L. Lien and J.-Y. Chang: *Sensor*, **22**, 3185 (2022).
12) S. Saggini, F. Ongaro, L. Corradini, and A. Affanni: *IEEE Trans. Emerg. Sel. Topics Power Electron.*, **3**, 766 (2015).
13) C.-C. Chang and J.-Y. Chang: *Microsys. Tech.*, **26**, 3421 (2020).
14) Y.-H. Chen, C. Lee, Y.-J. Wang, Y.-Y. Chang, and Y.-C. Chen: *Micromachi.*, **13**, 623 (2022).
15) K. Takahashi, A. Takebuchi, T. Yamada, and Y. Takemura: *J. Mag. Soc. Jpn.*, **42**, 49 (2018).
16) C. Yang, T. Sakai, T. Yamada, Z. Song, and Y. Takemura: *Sensors*, **20**, 1408 (2020).

Fig. 9 Left vertical axis; Energy consumption by load resistance (E_{load}, orange), hysteresis loss ($E_{hysteresis}$, blue), and energy consumption by internal resistance ($E_{internal}$, green) under applied AC magnetic field of $\mu_0 H = 3–13$ mT at 1 kHz. Connected load resistance was $R = 30, 100, 300,$ and 1000 Ω. Right vertical axis; energy efficiency consumed by load resistance (red bold circle).

<Paper>

Development of Cylindrical Linear Actuator for Vertical Transfer: Fundamental Consideration of Effect of Shape on Thrust Characteristics

H. Nosaka, D. Uchino, K. Ogawa*, T. Kato**, K. Ikeda***, A. Endo****, T. Narita, and H. Kato

Tokai Univ., *4-1-1 Kitakaname, Hiratsuka-shi, Kanagawa 259-1292, Japan*

* Aichi University of Technology, *50-2 Manori, Nishihasama-cho, Gamagori-shi, Aichi 443-0047, Japan*

** Tokyo University of Technology, *1404-1 Katakuramachi, Hachioji-shi, Tokyo 192-0982, Japan*

*** Hokkaido University of Science, *7-15-4-1 Maeda, Teine-ku, Sapporo-shi, Hokkaido 006-8585, Japan*

**** Fukuoka Institute of Technology, *3-30-1 Wajiro-higashi, Higashi-ku, Fukuoka-shi, Fukuoka 811-0295, Japan*

In conventional elevators, vibration and twisting of the cable become a serious problem when the cable is long. Therefore, an elevator that omits the counterweight and is moved by an actuator on a single cable with both ends fixed has been considered. However, contact decreases the efficiency and damages the cable owing to the inclusion of foreign matter. Therefore, a vertical transportation system is proposed that moves above a long, uniform conductor cable without contact by using a cylindrical linear induction motor (LIM) as the actuator. A cylindrical LIM above the reaction plate, which is a cylindrical shell-shaped conductor, has the advantage that the magnetic force acts on the reaction plate uniformly. This suppresses the vibration in the gap direction. However, a conventional LIM drives the mover in the horizontal direction. Therefore, a model was constructed for analyzing the cylindrical LIM for vertical transfer, and electromagnetic field analyses were performed using the finite-element method. The thickness of the reaction plate was varied, and the effect on the generated thrust was investigated. The optimal thickness of the cable was determined from the results by obtaining the range of the magnetic flux density acting on the cable.

Key words: magnetic recording, soft magnetic material, superconductor, magneto-optical recording, thin film

1. Introduction

In buildings and structures with multiple levels, elevators are essential to transport people and materials vertically through these levels. A schematic diagram of a conventional elevator is shown in Fig. 1(a). A conventional elevator consists of a cargo carrying people and materials, a counterweight of approximately the same weight as the cargo, a tether connecting the cargo and counterweight, and two pulleys supporting the tether. A motor is attached to either the upper or the lower pulley to provide the power necessary for lifting and lowering. In recent years, many large buildings with heights of several hundred meters have been constructed. However, the cables in large buildings are extremely long, and vibration and twisting of the cables become serious problems[1,2]. In addition, because conventional elevators attach one cargo to one tether, the area occupied by the elevator at a certain level in a high-rise building becomes large. Therefore, we are considering an elevator that does not use a counterweight and uses an actuator to raise and lower the cargos on a single tether with fixed ends, as shown in Fig. 1(b). This method allows multiple cargos to be installed on a single tether and is expected to increase the transport volume[3].

On the other hand, space development has been actively carried out, and satellites or materials for space stations are transported by rockets. The problem with rockets is that they are extremely expensive to

transport, and the safety of the surrounding area is a concern if a launch failure occurs. A space elevator that connects the ground to a geostationary orbit of 36,000 km with a cable and transports materials by ascending and descending on the cable has been proposed. This research can be positioned as basic research on the actuator of the climber for the space elevator. Structures that cannot realistically be equipped with counterweights will become taller and taller, and space elevators will start to become a reality, making it difficult to install counterweights themselves in some cases.

As shown in Fig. 2[4]–[6], the climber for such an elevator uses rollers or tires driven by a rotating motor to generate a frictional force between the rollers and the cable. This frictional force causes the elevator to lift and lower. However, the elevator requires a frictional force that exceeds the weight of the object being lifted. There are several ways to generate a high frictional force, one of which is to increase the coefficient of friction by surface treatment of the cables or tires. Another is to increase the pressing force. However, these methods are less efficient when foreign objects are entrapped and cause damage to the cable surface. Furthermore, because the friction coefficient of a carbon nanotube, which is expected to apply to the tether of the space elevator, would be very few, a climber with a friction force would need a larger pressing force.

For vertical devices with long cables, a major challenge is to reduce maintenance and replacement. To extend the life of such devices, devices that can be raised and lowered without mechanical contact are

Corresponding author: T. Narita (e-mail: narita@tsc.u-tokai.ac.jp).

(a) Conventional elevator　(b) Elevator without counterweight
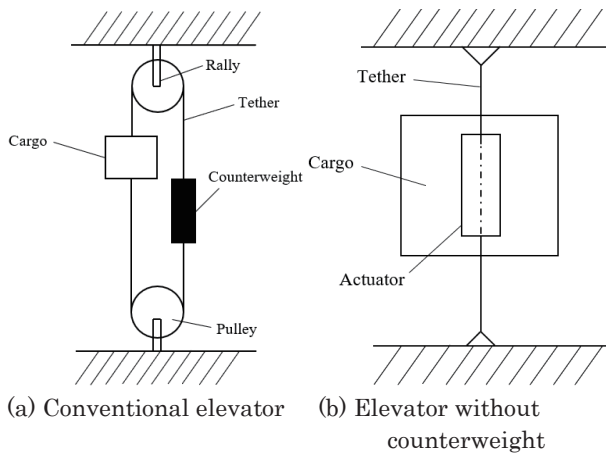
Fig. 1　Schematic diagram of elevator.
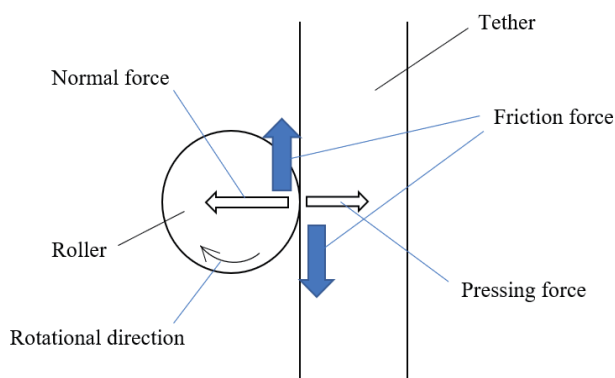
Fig. 2　Schematic diagram of friction force for vertical transfer in a conventional climber.

required. Linear synchronous motors and linear switched-reactance reactance motors are being investigated to realize such devices[7]. Linear induction motors (LIM), which can be driven without contact over a uniformly shaped reaction plate, have been applied as horizontal propulsion in railroads, maglev, sky rail, etc.[8),9)]. This study focuses on the characteristics of this LIM and examines its application to vertical movement, such as in elevators.

A typical LIM installed on a flat reaction plate is pressed against the reaction plate, and the gap between the LIM and the reaction plate changes. This causes the LIM to vibrate and to contact the reaction plate. Furthermore, a flat LIM has difficulty maintaining the gap against vibrations caused by various disturbances and torsion.

Furthermore, these LIM has a disadvantage as end effect and edge effect [10),11)]. On the other hand, a linear induction motor with a cylindrical primary has also been proposed[12)] .Compared to the flat plate type, this cylindrical LIM has no coil ends, which increases the main magnetic flux and improves the thrust and power factor. In addition, the axisymmetric structure cancels magnetic attractive forces and facilitates support[13)] .

In addition, a Z-θ drive actuator that can move not only in the axial direction but also in the

circumferential direction has also been proposed[14)] .

However, there has been no detailed study of the effect of the shape of the actuator that raises and lowers the long cable-like tether on the thrust characteristics.

Therefore, a cylindrical linear induction motor for vertical movement, in which a cable-shaped conductor with uniform geometry is moved vertically, was investigated in this study. The optimal tether shape is considered to vary depending on the structure of the building, assuming operation in a skyscraper.

In this study, to establish design guidelines for the parameters of the tether for vertical movement, the effect of varying the diameter of the tether, which serves as the reaction plate of the cylindrical LIM, on the thrust characteristics was examined.

2. Fundamental Study on Thrust Characteristics of Linear Actuators
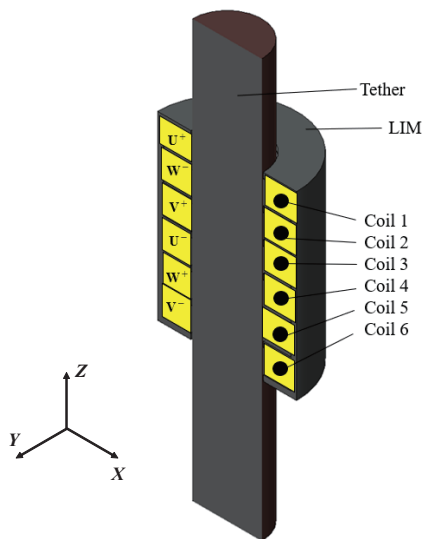
2.1 Analysis model

A schematic diagram of the proposed cylindrical LIM is shown in Fig. 3. This paper did not examine the shape of the tether for a LIM of a certain shape, but focused on how the thrust characteristics change when the shape of the LIM itself is changed. While a hollow tether was used for the study in the previous paper, the study in this paper was conducted from a model with a very small tether diameter. Since the magnetic field from the opposing coil may affect the thrust characteristics, an analytical model with a solid medium tether is constructed as a basic study. The climber is operated from an external power supply and has a system such that in the event of a loss of power, this mechanical brake is activated to stop the climber on the cable. It is necessary to consider how to feed power to the coils from the outside while the climber is elevated, and how efficient the proposed linear motor is in terms of electric power. An overview of the LIM analytical model is shown in Table 1. The cylindrical linear induction motor consists of a core, bobbin, and coil, and it has an outer diameter of 80 mm, an inner diameter of 32 mm, and a height of 130 mm. The material used for the core is S45C, the bobbin is plastic, and the coil is Cu. The coils are installed at six locations inside the core of the climber, and each coil is connected to a three-phase AC power supply, as shown in Fig. 4. The tether material is copper, and the frequency output from the power supply is changed to calculate the thrust characteristics acting on the climber by analysis. In this study, an analytical model of the LIM was created, and a magnetic field analysis was conducted to understand the lifting and lowering performance and thrust characteristics of the non-contacting climber. The LIM model is shown in Fig. 5. The radial direction of the LIM is defined as the X-axis and Y-axis, and the axial direction of the cable is defined as the Z-axis.
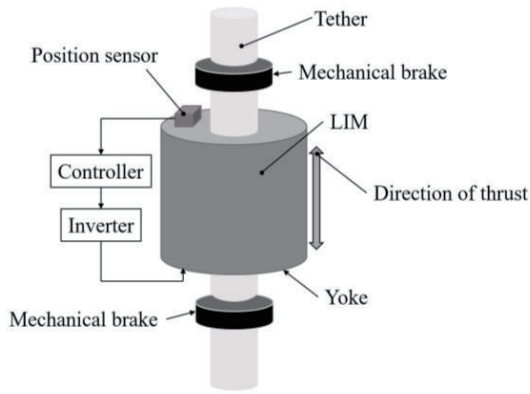
Fig. 3 Schematic diagram of proposed climber using LIM.
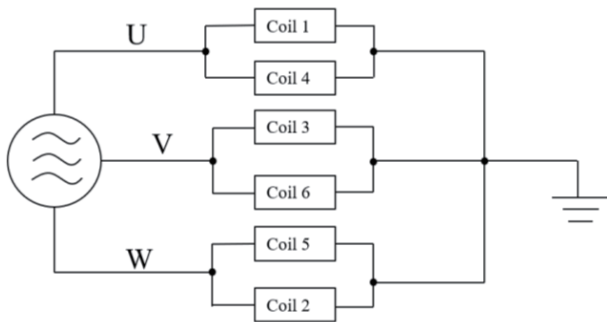
Fig. 4 Circuit diagram of the LIM analysis model.

Fig. 5 Analysis model of cylinder-type noncontact climber.

Table 1 Specifications of analysis model.

	Core	S45C
Material	Bobbin	Plastic
	Coil	Cu
	Tether	Cu
LIM	Inner diameter d_i	32 mm
	Outer diameter d_o	80 mm
	Height	130 mm
	Mass	4.3 kg
Tether	Diameter d_t	30 mm
Number of coils		6
Air gap		1 mm

Table 2 Analysis conditions.

Parameters	Values
Current Amplitude	7.85 $A_{0\text{-}p}$
Frequency	1-100 Hz

Fig. 6 Top view of model.

is 0.62 Ω. The model self-weight under each analysis condition was calculated based on the specifications shown in Table 1 for the bias of the analytical model. The analysis conditions are shown in Table 2. 7.85 A was used for current amplitude of the three-phase AC power supply to set the coil current density to 10 A/mm² and the frequency to 1–100 Hz, and an electromagnetic field transient response analysis was performed. The analysis time was approximately 0.05 s, with time increments of 0.005 s for each calculation step. The electromagnetic force generated in the Z-axis direction, which is the axial direction of the tether, was assumed to be the thrust force.

2.3 Analysis results

The average thrust force at each frequency obtained from the electromagnetic field analysis are shown in Fig. 7. The figure shows that the vertical thrust was obtained at all frequencies, that the thrust increased as
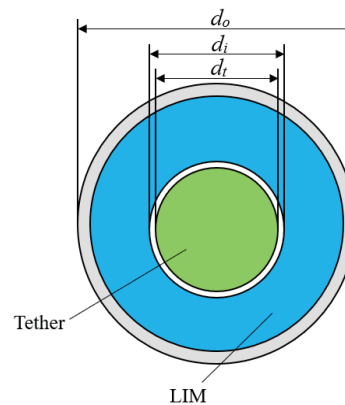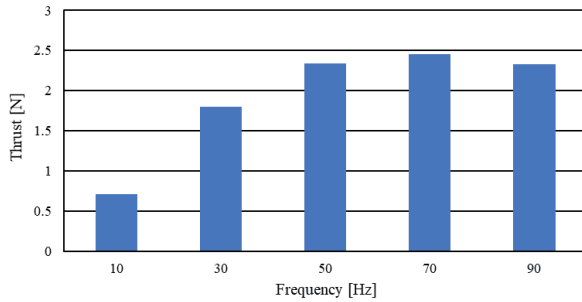
2.2 Analysis conditions

To evaluate the lifting and lowering performance of an LIM as a climber, the thrust that can be generated was compared with the mass of the climber itself. The circuit diagram of the LIM to be analyzed is shown in Fig. 4. The winding diameter of the coil in the slot of the model was set to 1 mm, and the number of turns was set to 182 to achieve a fill factor of 50%. The winding

Fig. 7 Analyzed average thrust force (d_t = 30 mm).

Table 3 Model specifications.

Model		A	B	C	D
Material	Core		S45C		
	Bobbin		Plastic		
	Coil		Cu		
	Tether		Cu		
LIM	Tether diameter d_t	10 mm	20 mm	30 mm	40 mm
	Inner diameter d_i	12 mm	22 mm	32 mm	42 mm
	Outer diameter d_o	60 mm	70 mm	80 mm	90 mm
	Height	130 mm	130 mm	130 mm	130 mm
	Mass	2.9 kg	3.6 kg	4.3 kg	5.0 kg
	Weight	29 N	36 N	43 N	50 N
Number of coils			6		
Air gap			1 mm		

Table 4 Analysis conditions.

Model	A	B	C	D
Tether diameter d_t [mm]	10	20	30	40
Frequency f [Hz]	10-500	10-200	10-100	10-100
Step time [s]	0.0001	0.00025	0.0005	0.0005
Number of steps	501	201	101	101

the frequency increased, and the effect of transients also increased. The same figure shows that the average value of the thrust also increases as the frequency increases, but the effect of transients also increases. Furthermore, the average value of the thrust increases with increasing frequency, but the thrust decreases after 70 Hz.

3. Effect of Tether Outside Diameter on Thrust Characteristics of Linear Actuators

3.1 Analytical model

Because of the structure of the elevator under consideration, it is possible that multiple cargos may be raised and lowered on a single tether. The required tether strength may vary depending on the height of the structure. In other words, the tether diameter is considered to vary depending on the operating conditions of the elevator. Therefore, the thrust characteristics of an LIM moving up and down on a tether were studied when the tether diameter was changed. The tether diameters dt were 10, 20, 30, and 40 mm. Four LIM models, A–D, were designed

according to the tether diameter. Table 3 shows the characteristics of each LIM analytical model. An overview of the analytical model described in Section 2, which corresponds to Model C, is shown in Fig. 8.

3.2 Analysis conditions

Four models were analyzed, with the tether diameter varied in 10-mm increments. Table 4 shows the analysis conditions for each model. All models were analyzed with a current of 7.85A and 182 turns per coil. However, preliminary results showed that the frequency at which the maximum thrust was achieved varied depending on the tether diameter, so the frequency and number of steps were changed for each model as shown in Table 4.

3.3 Analysis results

Vector plots of the magnetic flux density, vector plots of the current density, and contour plots of the Lorentz force density for each model are shown in Figs. 9–11. The magnetic flux and current results indicate that a large Lorentz force is generated. Furthermore, as the tether diameter increased, the area inside the tether where the Lorentz force was not generated increased.

The average thrust of each model after 0.02 s is shown in Fig. 12. The horizontal axis of the graph shows the frequency, and the horizontal axis shows the thrust. Based on these results, the relationship between tether diameter and Thrust-to-weight ratio is shown in Fig. 13. This figure shows that, as the tether diameter increases, and the thrust-to-weight ratio increases accordingly, and the frequency at which the highest thrust is obtained decreases.

4. Conclusion

A vertical transport system using a cylindrical LIM as an actuator was studied. It can move over a uniform conductor cable without contact. The thrust characteristics of the system were also studied when the tether diameter was changed. The analysis results show that, as the tether diameter increases, the thrust generated in the climber tends to increase, and the frequency at which the maximum thrust is obtained tends to decrease. Also, increasing the diameter tended to increase the thrust more than the increase in the surface area of the gap, and the thrust was obtained more efficiently.

Future studies are planned in which the area of the slot where the coil is wound, the aspect ratio of the coils, and the distance between the coils are changed to obtain a higher thrust force. It is also necessary to study the possibility of obtaining higher thrust by changing the materials of the core and tether to materials with a high-saturation magnetic flux density or different electrical resistivity.

In addition, it is necessary to conduct a detailed study from the viewpoint of method of power supply and energy efficiency.
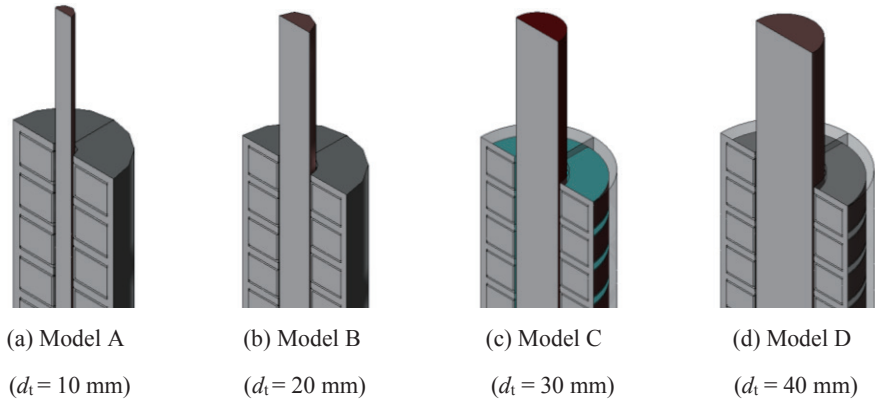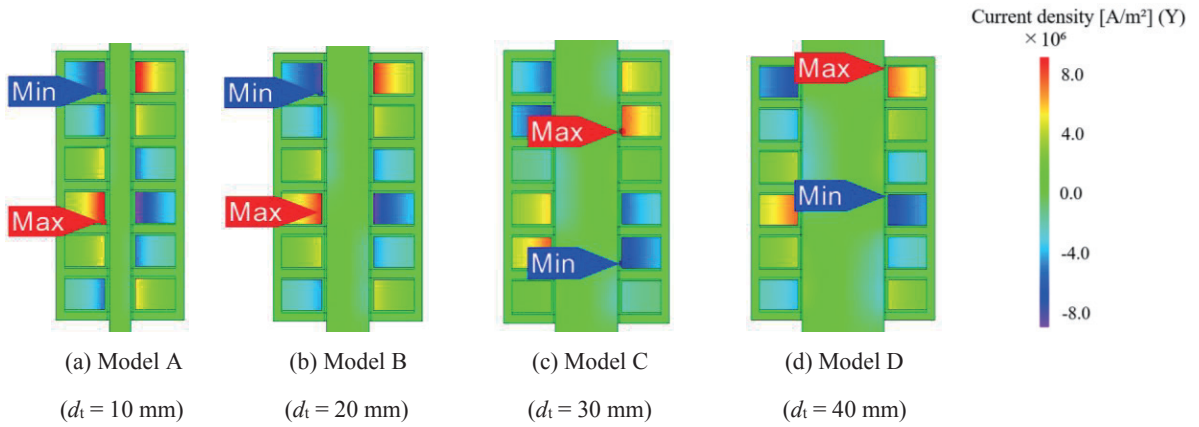
(a) Model A
(d_t = 10 mm)

(b) Model B
(d_t = 20 mm)

(c) Model C
(d_t = 30 mm)

(d) Model D
(d_t = 40 mm)

Fig. 8 Analysis model in each cable thickness.

(a) Model A
(d_t = 10 mm)

(b) Model B
(d_t = 20 mm)

(c) Model C
(d_t = 30 mm)

(d) Model D
(d_t = 40 mm)

Fig. 9 Analyzed current density in each tether diameter.

(a) Model A
(d_t = 10 mm)

(b) Model B
(d_t = 20 mm)

(c) Model C
(d_t = 30 mm)

(d) Model D
(d_t = 40 mm)

Fig. 10 Analysed magnetic flux density.

(a) Model A
(d_t = 10 mm)

(b) Model B
(d_t = 20 mm)

(c) Model C
(d_t = 30 mm)
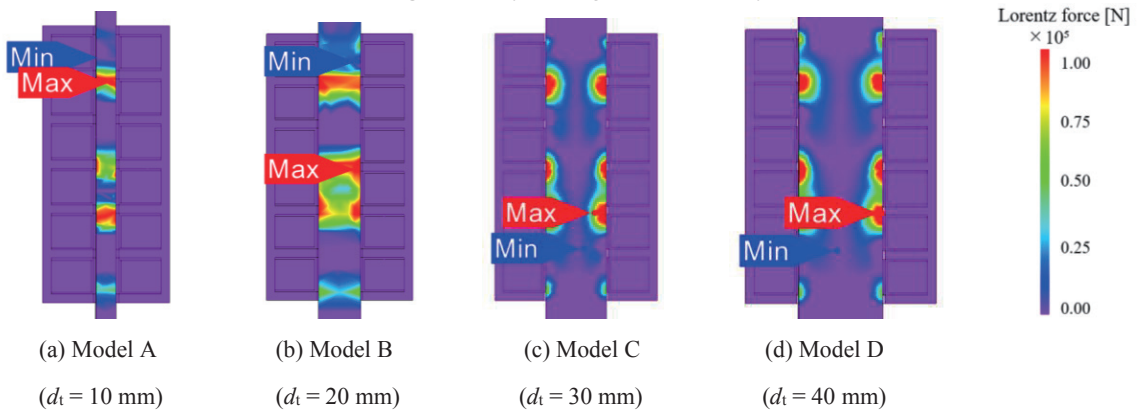
(d) Model D
(d_t = 40 mm)
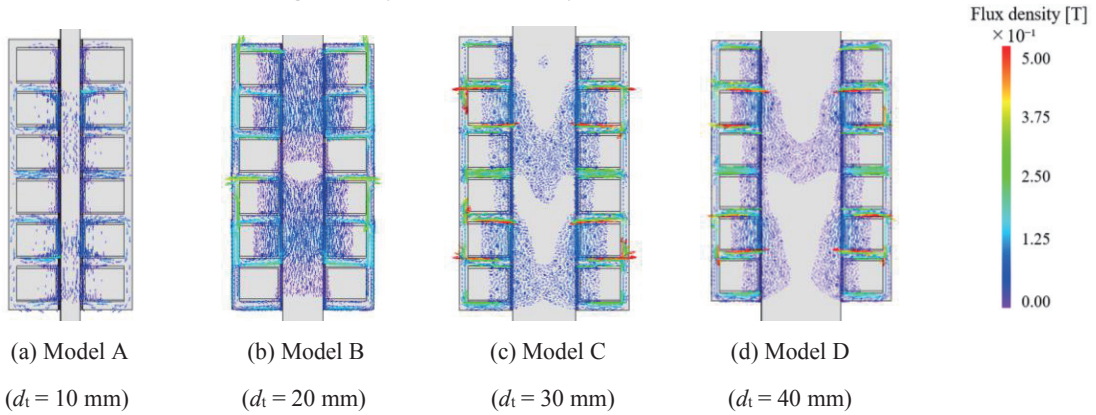
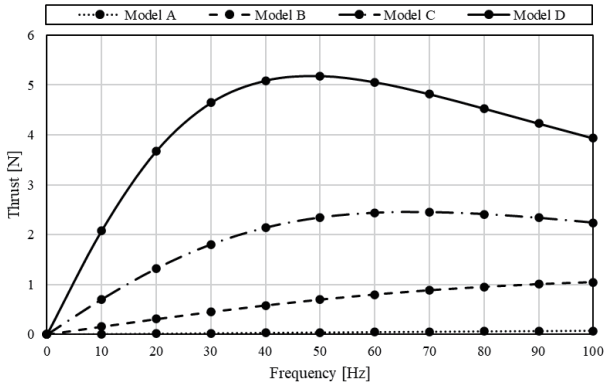**Fig. 11** Contour plot of analysed Lorentz force.
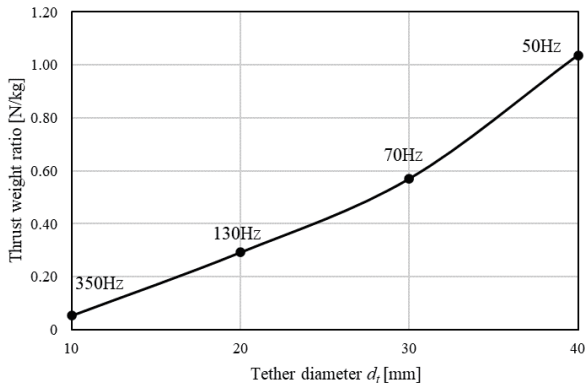
Fig. 12 Average thrust.

Fig. 13 Thrust-to-weight ratio of the maximum thrust of each model to its own weight.

References

1) T. Fujitani and H. Kimura: *Trans. JSME*, **89**, 18-00048 (2018).
2) S. Jia: *Powder Technol.,* **320**, 462 (2017).
3) T. Matsuno: *J. Soc. Control Instrum. Eng.*, **21**, 717 (1982).
4) Y. Ishikawa, K. Otsuka, Y. Yamagiwa, and H. Doi: *Acta Astronaut.*, **145**, 165 (2018).
5) K. Ishizaki, K. Soonsu, F. Inoue, E. Omoto, and Y. Ishikawa: *JSMERMD, The Proceedings JSME annual Conference on Robotics and Mechatronics*, Yokohama, Japan, 2016, **2A2-17b2** (JSME, Tokyo, 2017).
6) Y. Aoki: *Aeronautical and Space Sci. Jpn.*, **62**, 325 (2014).
7) R. Coa, E. Su, and M. Lu: *IEEE Trans. Appl. Supercond.*, **30**, 3601205 (2020).
8) S. Watanabe, T. Koseki, Y. Noda, and M. Miyatake: *IEEJ Trans. Ind. Appl.*, **137**, 44 (2017).
9) T. Mizuno: *IEEJ Trans. Ind. Appl.*, **120**, 479 (2000).
10) S. Yamamura, H. Ito and Y. Ishikawa: *IEEJ J. Inst. Electr. Eng. Jpn.*, **91**, 309 (1971).
11) T. Onuki, H. Numata, and T. Yamamura: *IEEJ J. Ind. Appl.*, **110**, 807 (1990).
12) T. Morizane, T. Koseki, E. Masuda: *IEEJ J. Ind. Appl.*, **112**, 1149 (1992).
13) A. Hirano, N. Maki, and Y. Tanaka: *IEEJ J. Ind. Appl.*, **122**, 871 (2002).
14) E. Amiri: *IECON 2014 - 40th Annual Conference of the IEEE Industrial Electronics Society*, Dallas, TX, USA, 2014, pp. 431-436 (IEEE, Piscataway, New Jersey, 2015).

<Paper>

Linear Actuators for High-Speed Reciprocating Motion with Dual Halbach Arrays
(Fundamental Consideration of the Effect of Magnet Arrangement on Thrust Characteristics)

M. Tanaka, K. Kimura, J. Kuroda, Y. Majima, D. Uchino, K. Ogawa,
T. Kato*, K. Ikeda**, A. Endo***, T. Narita and H. Kato

Tokai Univ., *4-1-1 Kitakaname, Hiratsuka-shi, Kanagawa, 259-1292, Japan*
Tokyo University of Technology, 1404-1 Katakuramachi, Hachioji-shi, Tokyo 192-0982, Japan
** Hokkaido University of Science, *7-15-4-1 Maeda, Teine-ku, Sapporo-shi, Hokkaido, 006-8585, Japan*
*** Fukuoka Institute of Technology, *3-30-1 Wajiro-higashi, Higashi-ku, Fukioka-shi, Fukuoka, 811-0295, Japan*

To achieve higher performance in spark-ignition engines, the intake and exhaust valves must be controlled in a stepless manner according to the engine speed. Our research group has been continuously studying the electromagnetic drive valve system using a linear actuator. We designed a linear actuator with a dual Halbach array of permanent magnets in the stator to increase the thrust of the linear actuator. The thrust characteristics of the proposed model were investigated using electromagnetic field analysis based on the finite element method. The analysis confirmed that the Halbach array concentrates the magnetic flux on the coil side, which generates Lorentz force. From the analysis results, the proposed liner actuator can generate thrust for driving the engine valve, and optimal permanent magnets in stator can be obtained to generate higher thrust.

Keywords: liner motor, valve drive system, reciprocating engine, dual Halbach array

1. Introduction

Reciprocating motion is used at various points in the operation of mechanical products. Generally, reciprocating motion is converted from the rotational motion of a motor or engine by a mechanism, such as a cam or a piston/crank mechanism. However, direct drives with linear actuators must utilize high-precision and high-speed reciprocating motion. [1]–[5]

For example, the cylinder head of an internal combustion engine (ICE) has intake and exhaust engine valves. These valves are opened and closed using linear motion converted by the camshafts that are rotated by the engine. The cam geometry determines the commanded motion of the valves, i.e., when and how wide to open and when to close them. The cam shape is a parameter that significantly affects the engine's combustion and thus directly affects the performance of the ICE, such as power output and fuel consumption. In a typical engine, the engine is operated with a single cam profile, so there are areas where the cam profiles do not match depending on the rpm of operation, resulting in poor engine performance. A mechanism that switches cam profiles according to the operating speed has been proposed to solve this problem. [6] [7] This system has been implemented in sports cars to improve driving performance and in some production cars to improve fuel economy. However, these systems rely on multiple cam

shapes. The engine valves can always be operated with optimal parameters according to the continuously changing speed of the ICE. In addition, these systems' cam shapes, or engine valve operation patterns, are designed with restrictions to avoid mechanical problems such as surging and valve jumps.

Therefore, a method has been proposed to operate the engine valve with a linear actuator without involving the cam mechanism. This system can operate the engine valve optimally according to the engine speed without mechanical limitations. In addition, the output can be varied in response to accelerator pedal operation without needing a throttle valve. This improves the combustion of the ICE engine and can be expected to increase power output and fuel consumption. Several studies have proposed linear actuators to drive engine valves, focusing on this advantage. [8]–[12] However, in these studies, although sufficient yokes were installed on the mover, it is difficult to operate the actuator precisely at the speed required for ICE engines because of its high inductance and heavy mover. Therefore, there is a need to develop a compact linear actuator that can provide high thrust.

The gap magnetic flux must be increased to realize a high thrust actuator in a limited space, such as inside a cylinder head. Therefore, this research focused on a cylindrical moving coil linear actuator with a lightweight mover and small ink dance. In addition, a Halbach array was used for the stator's permanent magnet array to increase the gap magnetic flux. A dual Halbach array was used to further increase the flux density of the permanent magnets, with Halbach magnet rows on the inner and outer sides of the moving coil. However, there

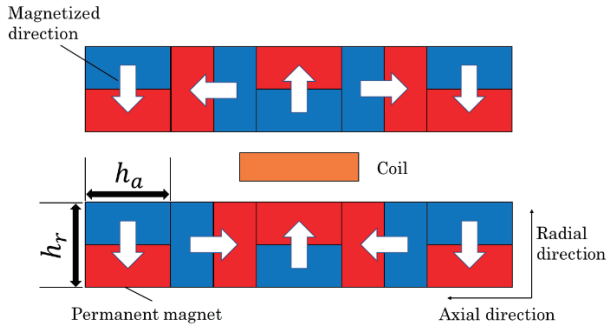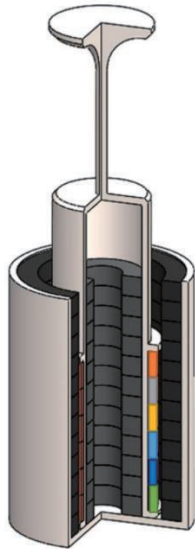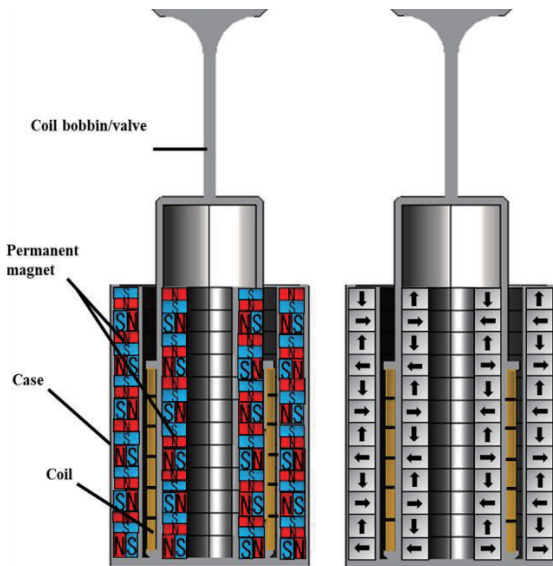Corresponding author: T. Narita
(e-mail: narita@tsc.u-tokai.ac.jp).

Fig. 1 Schematic of dual Halbach array.

(a) Bird's view

(b) Dual Halbach model (c) Magnetization direction

Fig. 2 Analysis model.

are few examples of this method being used for reciprocating actuators, and no detailed studies have been conducted. In addition, the diameters of the inner
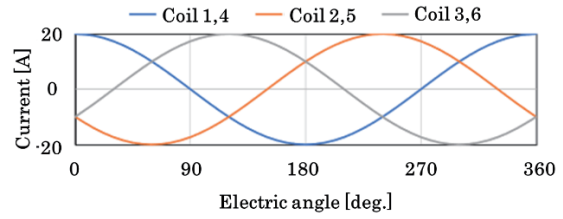

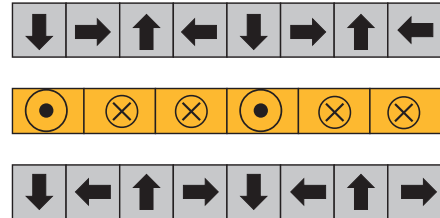**Fig. 3** Input three-phase alternating current.

Fig. 4 Current directions in each coil.

and outer magnets are different in the cylindrical type, and the volume of the magnets is considered to be different, resulting in unequal magnetic flux. Therefore, this paper presents an electromagnetic field analysis of the changes in thrust characteristics of a cylindrical linear actuator by changing the size of the outer permanent magnet array.

2. Analysis model of the actuator using dual Halbach array

2.1 Outline of dual Halbach array

The linear actuator uses Fleming's left-hand rule to generate Lorentz force by orthogonalizing the magnetic flux in the coil to obtain thrust. Therefore, the thrust force can be increased by increasing the orthogonal magnetic flux through the coil by changing the direction of magnetization for each permanent magnet.

The dual Halbach array, which concentrates the magnetic flux in the coil by changing the direction of magnetization for each permanent magnet, comprises two types of magnets, as shown in Fig. 1. They include a radially oriented magnet that makes the magnetic flux orthogonal to the coil and an axially oriented magnet that guides the magnetic flux from one radially oriented magnet to another to prevent the flux from going outside the motor. The radially oriented magnets are used in the motor. In previous studies, the radial and axial magnets had the same thickness. Therefore, we considered that the thrust could be increased by increasing the thickness of the radial magnet, which directs the magnetic flux orthogonally to the coil.
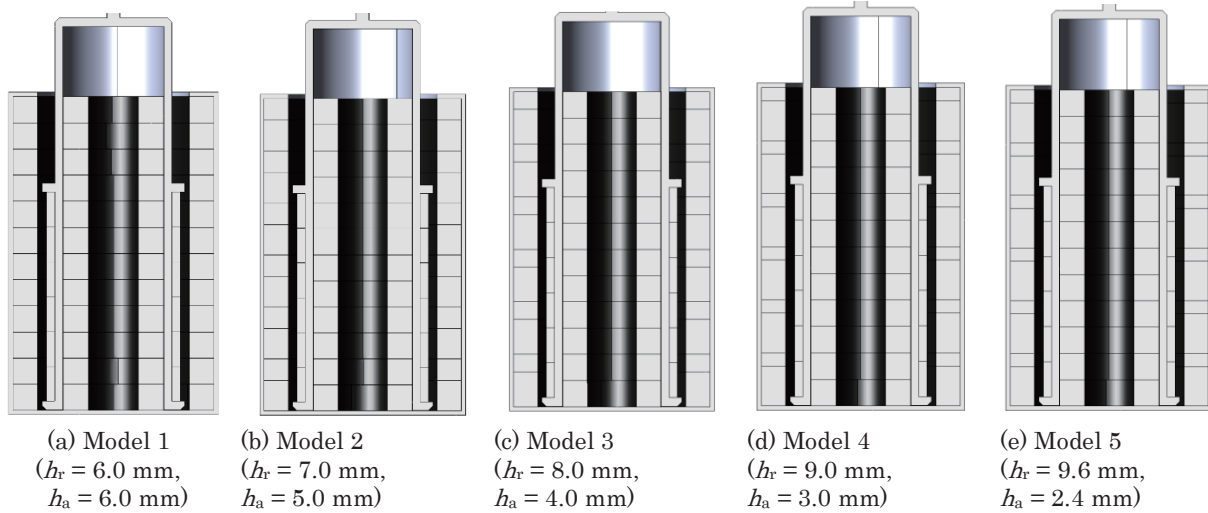
2.2 Linear actuator using Halbach array

To investigate changes in the thrust characteristics by changing the aspect ratio of the permanent magnet, an analytical model was created using the 3D CAD software SOLIDWORKS, as shown in Fig. 2. Fig. 2 (a) shows a birds view of our proposed linear actuator. Fig. 2 (b)

Table 1 Specifications of permanent magnets

Model	1	2	3	4	5
Thickness of permanent magnet magnetized in radial direction h_r [mm]	6.0	7.0	8.0	9.0	9.6
Thickness of permanent magnet magnetized in axial direction h_a [mm]	6.0	5.0	4.0	3.0	2.4

(a) Model 1
(h_r = 6.0 mm,
h_a = 6.0 mm)

(b) Model 2
(h_r = 7.0 mm,
h_a = 5.0 mm)

(c) Model 3
(h_r = 8.0 mm,
h_a = 4.0 mm)

(d) Model 4
(h_r = 9.0 mm,
h_a = 3.0 mm)

(e) Model 5
(h_r = 9.6 mm,
h_a = 2.4 mm)

Fig. 5 Analysis model of liner actuator applying dual Halbach array.

Table 2 Specifications of analysis model.

Parts	Dimension	Values
Case	Outer diameter	49.0 mm
	Height	70.0 mm
	Thickness	2.0 mm
Outer magnet	Inside diameter	34.8 mm
	Outer diameter	40.8 mm
Inner Magnet	Inside diameter	11.2 mm
	Outer diameter	22.5 mm
Coil bobbin	Inside diameter	6.4 mm
	Outer diameter	10.4 mm
	Height	72.0 mm
	Thickness	2.0 mm
Coil	Inside diameter	26.3 mm
	Outer diameter	32.0 mm
	Height	7.5 mm

Table 3 Materials in each part of analysis model.

Parts	Materials
Coil bobbin	YEP-B (Permalloy)
Value	YEP-B (Permalloy)

was applied to each coil. Coils 1 and 4 were set to U phase, Coils 2 and 5 to V phase, and Coils 3 and 6 to W phase as shown in Fig. 4. The current directions in each coil were shown in Fig. 4. A case is placed outside the valve, bobbin, and outer permanent magnet. In this analytical model, the coils, valves, and bobbins act as moving parts.
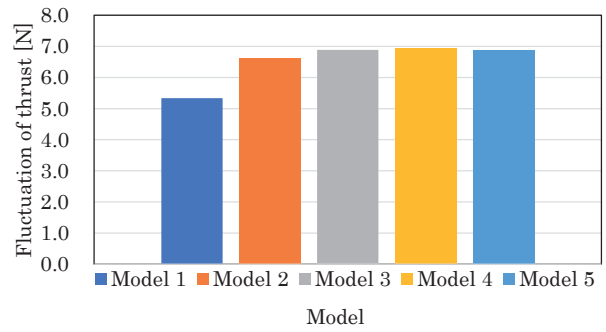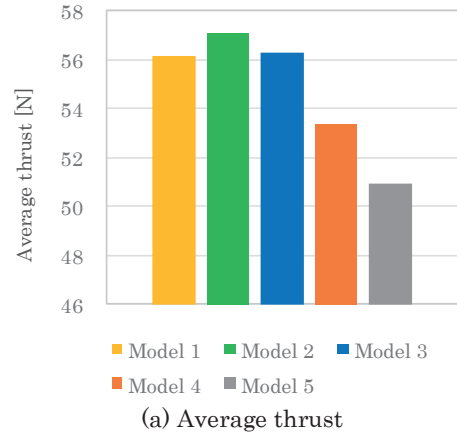
3. Effect of magnet shape on thrust characteristics

3.1 Analysis conditions

The area of radial permanent magnets located outside the coil was increased in steps, and the area of axial permanent magnets was decreased accordingly to increase the radial magnets' thickness without changing the linear actuator's size or the number of permanent magnets. The permanent magnets' thicknesses were varied in steps up to 9.6 mm in the radial direction and 2.4 mm in the axial direction, with the basic model having a radial thickness of h_r and an axial thickness of h_a of 6.0 mm. The dimensions of each model are shown in Table 1. The model specifications are shown in Table 2; materials were set as shown in Table 3, and Fig. 5 shows the analytical model. The number of turns elements in this analysis model was almost 700,000. The number of turns of each coil was set to 33 turns. A three-phase

shows a cross-sectional view of the analytical model. Six cylindrical coils and 12 cylindrical permanent magnets were placed outside and inside the coils, respectively. The permanent magnets and the outer case constitute the stator. Fig. 2 (c) shows the magnetization direction of the permanent magnet. The coils are numbered from 1 to 6 in order from the top. Three-phase alternating current

(a) Model (h_r = 6.0 mm, h_a = 6.0 mm)

(b) Model 2 (h_r = 7.0 mm, h_a = 5.0 mm)

(c) Model 3 (h_r = 8.0 mm, h_a = 4.0 mm)

(d) Model 4 (h_r = 9.0 mm, h_a = 3.0 mm)

(e) Model 5 (h_r = 9.6 mm, h_a = 2.4 mm)
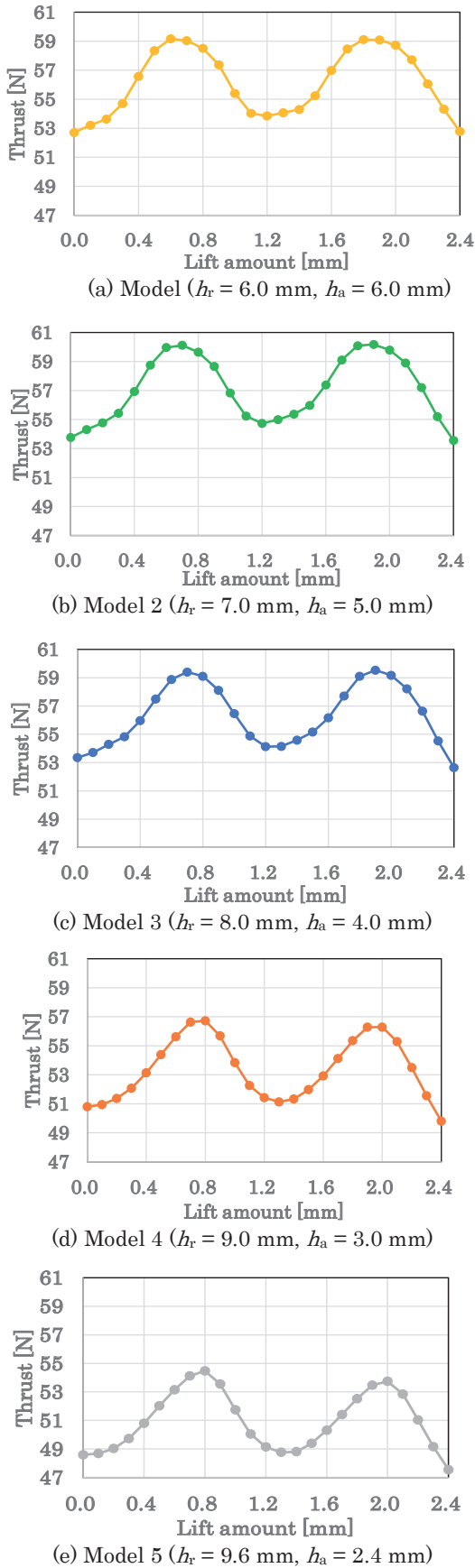
Fig. 6 Relationship between lift amount and thrust in each analysis model.

(a) Average thrust

(b) Fluctuation of thrust

Fig. 7 Analyzed results in each model.

alternating current was applied to each coil. Coils 1 and 4 were set to U phase, Coils 2 and 5 to V phase, and Coils 3 and 6 to W phase. The amplitude of the current was set to 20 A. In this actuator, 360° of electric angle means 2.4 mm displacement in the axial direction.

Electromagnetic analysis software (JMAG) was used for analysis. The number of steps in the analysis was 25, and the displacement of each step was 0.1 mm to obtain the thrust generated at each step.

3.2 Analysis Results

Fig. 6 shows the relationship between thrust and lift amount for each model, with the vertical axis showing the thrust and the horizontal axis showing the lift amount. From the results, the thrust in each model shows the same tendency, and Model 2 with h_r = 7.0 mm and h_a =5.0 mm generates a higher thrust. The summarized analysis result is shown in Fig. 7. Fig. 7 (a) shows the average thrust. This figure shows that the increase in the radial thickness h_r more than 7.0 mm in the model, which was expected to increase flux density in the air gap, contrarily decreased the average thrust. Fig. 7 (b) shows the fluctuation of thrust obtained by different thrust forces between maximum and minimum values. In the view point of thrust fluctuation, there is no difference in each model. Fig. 7 shows a vector plot of the magnetic flux density at a lift of 1.9 mm, and Fig. 8 shows Lorentz force density. The vector plots of the flux density and Lorentz density for each model at 20 steps are shown in
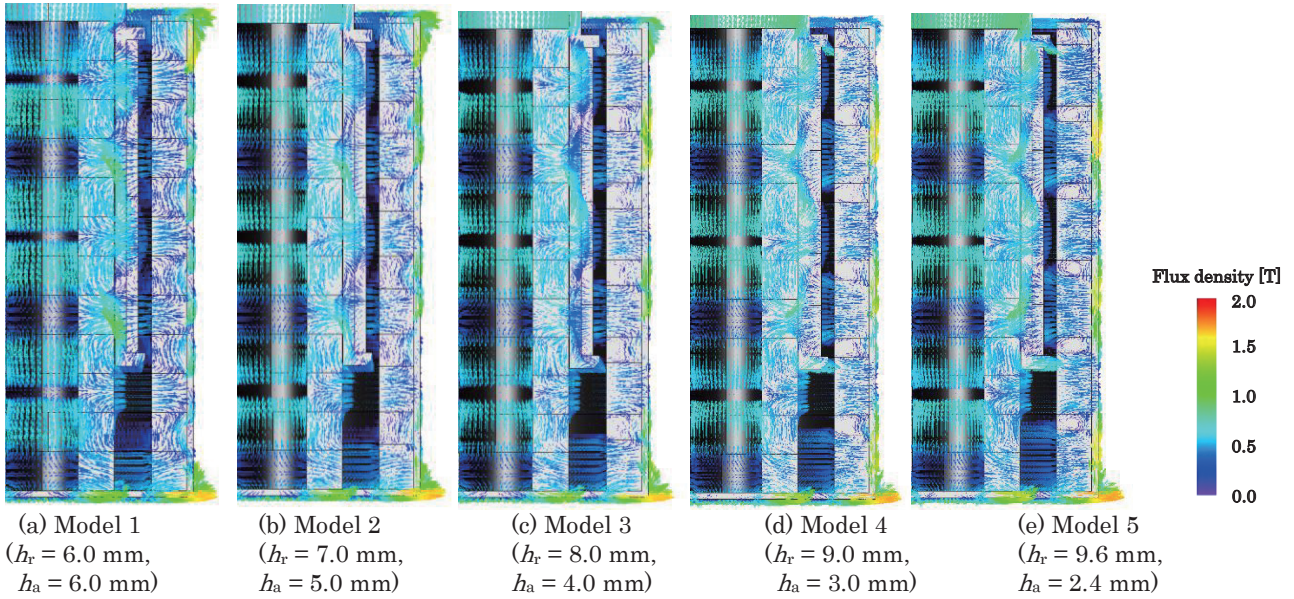
(a) Model 1
(h_r = 6.0 mm,
h_a = 6.0 mm)

(b) Model 2
(h_r = 7.0 mm,
h_a = 5.0 mm)

(c) Model 3
(h_r = 8.0 mm,
h_a = 4.0 mm)

(d) Model 4
(h_r = 9.0 mm,
h_a = 3.0 mm)

(e) Model 5
(h_r = 9.6 mm,
h_a = 2.4 mm)

Fig. 8 Analyzed flux density in each analysis model

(a)Model 1
(h_r = 6.0 mm,
h_a = 6.0 mm)

(b)Model 2
(h_r = 7.0 mm,
h_a = 5.0 mm)

(c)Model 3
(h_r = 8.0 mm,
h_a = 4.0 mm)

(d)Model 4
(h_r = 9.0 mm,
h_a = 3.0 mm)

(e)Model 5
h_r = 9.6 mm,
h_a = 2.4 mm)
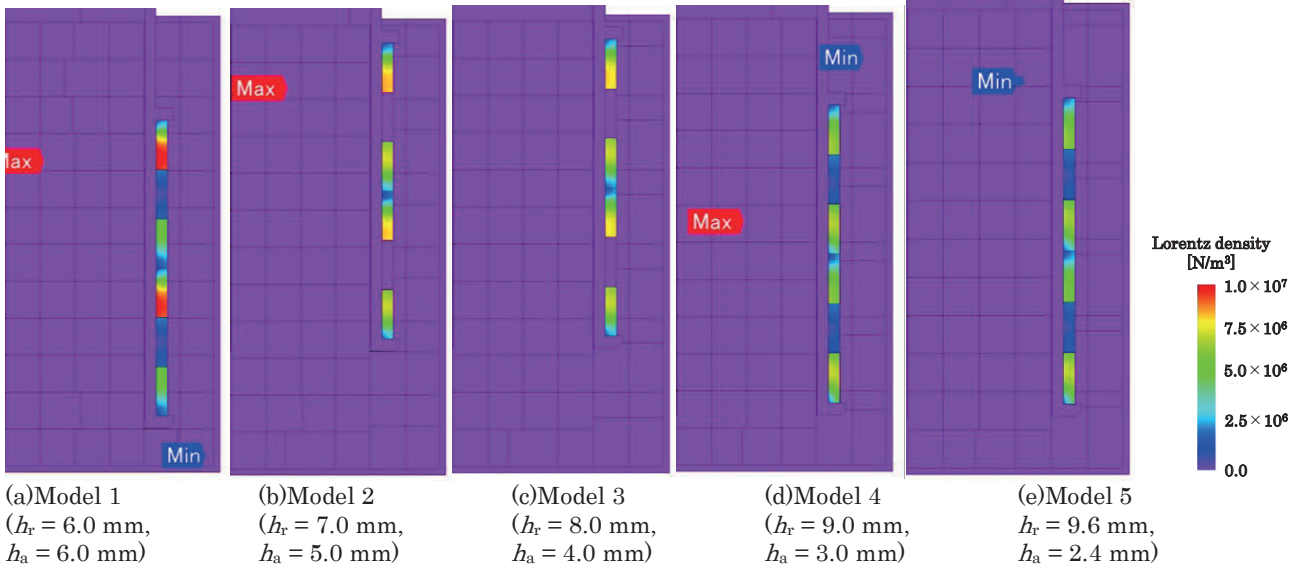
Fig. 9 Analyzed Lorentz force density in each analysis model

Fig. 8 and Fig. 9, respectively. The figures show that excessively increasing the radial permanent magnet area causes the magnetic flux to exit the case without passing through the axial permanent magnets. Therefore, in an actuator with a Halbach array, increasing the radial permanent magnet area, which makes the magnetic flux orthogonal to the coil, improves the thrust without changing the size of the actuator. However, the thrust was lower in Models 4 and 5, in which the radial permanent magnet the area was greater than in Model 1 with 6.0 mm axial and radial thickness.

4. Conclusion

We investigated the effect of a dual Halbach array on the thrust force of a linear actuator by altering the area of permanent magnets arranged in the actuator. In the Halbach array, the radial permanent magnet area that orthogonalizes the magnetic flux to the coil was increased, and the axial permanent magnet area that guides the magnetic flux out of the actuator was decreased. Consequently, a higher thrust force was generated than in the model with the same radial and axial permanent magnet regions. However, if the radial permanent magnet area is excessively increased, the axial permanent magnet cannot induce the magnetic flux, and the flux escapes to the outside of the case. In the future, various studies will be conducted to develop an actuator with an even higher thrust.

References

1) I. Martins, J. Esteves, G.D. Marques, and F.P. Da Silva: *IEEE Trans. Veh. Technol.* **55**, 86 (2006).

2) R. Kornbluh, R. Pelrine, J. Eckerle and J. Joseph: 1998 IEEE International Conference on Robotics and Automation, R. Kornbluh, Leuven, Belgium, 1998, **3**, pp.2147-2154 (IEEE, 1998)

3) F. Carpi, C. Salaris, and D. De Rossi: *Smart Mater. Struct.* **16**, S300 (2007).

4) M. Sakai, K. Hirata, and Y. Nakata: *Int. J. Appl. Electromagn. Mech.* **26**, 28 (2018).

5) Y. Keijiro, I. Masayuki, and M. Takasi: *Research Reports of Kanagawa Inst. Technol. B, Sci. and Technol.*, **21**, 33 (1997).

6) K. Hatano, K. Iida, H. Higashi, and S. Murata: *SAE Trans.* 1291 (1993).

7) T.H. Ma: *SAE trans.,* 665 (1988).

8) Y. Takao, M. Yoshifumi, and U. Masaki: *DENKI-SEIKO*, **74**, 147 (2003).

9) S. Akimoto, and A. Masaru: Conference of Tohoku Branch, The Japan Society of Mechanical Engineers, Japan, 2009, **44**, 172 (The Japan Society of Mechanical Engineers, 2009.)

10) O. Masaru, S. Akitomo, and K. Takahide: Conference of Tohoku Branch, The Japan Society of Mechanical Engineers, Japan, 2009, **44**, 174 (The Japan Society of Mechanical Engineers, 2009.)

11) M. A. Theobald, L. Bruno, and H. Rassem: *SAE Trans.* 1323 (1994).

12) S. Braune, L. Steven, and M. Paolo: 2006 IEEE Conference on Computer Aided Control System Design, 2006 IEEE International Conference on Control Applications, 2006 IEEE International Symposium on Intelligent Control., S. Braune, Munich, Germany, 2006, pp.1657-1662 (IEEE, 2006)

Editorial Committee Members・Paper Committee Members

Notice for Photocopying

編 集 委 員・論 文 委 員

複写をされる方へ

Journal of the Magnetics Society of Japan